

Chapter 15

Spectral Induced Polarization (SIP) Imaging for the Characterization of Hydrocarbon Contaminant Plumes



Adrián Flores-Orozco and Matthias Bucker

Abstract We review the application of the Spectral Induced Polarization (SIP) imaging method to delineate the geometry of hydrocarbon contaminant plumes and monitor the effect of remediation measures. In the first two sections, we present a brief introduction into the SIP method and discuss the electrical properties of the rocks and soils. In the third section, we offer a detailed revision of the literature to illustrate the broad range of electrical properties of fresh and mature contaminant plumes. In the fourth and fifth section, we discuss challenges and good practices for collection, processing and interpretation of SIP imaging data, and illustrate these steps with a real-case example regarding the characterization of a benzene plume. Along this case study, we demonstrate how the occurrence of benzene in the dissolved plume and in free-phase changes the electrical conductivity and polarization properties of the contaminated subsurface materials. A second case study deals with SIP monitoring results obtained along the injection of zero-valent iron particles for the remediation of a TCE (Trichloroethylene) plume. This example illustrates the advantages of the SIP method to evidence changes in the pore-space, such as clogging and fracking, which may affect the effectivity of remediation measures.

15.1 Spectral Induced Polarization (SIP) Imaging

Induced polarization (IP) refers to a geophysical method, which quantifies the capacity of rocks and sediments to conduct electrical current and accumulate electrical charges. To carry out an IP measurement, a pair of electrodes (e.g., metallic bars) is used to inject an electrical current into the ground, while another pair of

A. Flores-Orozco (✉)

Research Unit of Geophysics—Department of Geodesy and Geoinformation, Technical University of Vienna (TU-Wien), Wiednerhauptstrasse 8—10, 1040 Vienna, Austria
e-mail: adrian.flores-orozco@geo.tuwien.ac.at

M. Bucker

Institute of Geophysics and Extraterrestrial Physics, Technische Universität Braunschweig, Mendelssohnstraße 3, 38106 Braunschweig, Germany
e-mail: m.buecker@tu-braunschweig.de

electrodes is used to measure the resulting voltage (Fig. 15.1a). IP measurements can be collected in time domain (TDIP) by measuring decaying voltages directly after a direct current is shut off (Fig. 15.1b); or in frequency domain (FDIP) by injecting a sinusoidal current and voltage readings, typically in the frequency range between 10 MHz and 10 kHz (Fig. 15.1c). TDIP data is commonly expressed in terms of the transfer resistance (R , given by the voltage-to-current ratio) and the integral chargeability (m , given by the integrated voltage decay). In FDIP, the measurements are expressed in terms of a complex-valued electrical impedance (Z), characterized by a magnitude ($|Z|$, corresponding to the voltage-to-current ratio, or transfer resistance $|Z| = R$) and the phase shift between the current and the voltage. The use of sinusoidal currents at different frequencies results in an impedance spectrum. This approach, which evaluates the frequency dependence of the electrical properties, is referred to as spectral induced polarization (SIP).

Under certain conditions, SIP data can be extracted from TDIP measurements (e.g., Fiandaca et al. [22]), especially if TDIP measurements are conducted with different pulse lengths (for current injection and the recording of the integral chargeability), this conversion yields good results. Based on this idea, the DAS-1 (from Multi-Phase Technologies, MPT) is a measuring device, which permits the collection of both TDIP and FDIP data. Other instruments, e.g., the latest Terrameter LS2 from ABEM, digitize the full voltage decay (also known as “full wave form”) at high sampling rates. If used in conjunction with suitable modeling algorithms, spectral parameters can be inverted directly from the full-waveform TDIP data. Although this approach has shown to yield good results under certain conditions, only the repetition of FDIP measurements at different frequencies or TDIP measurements with different pulse lengths enables a direct determination of the frequency-dependent electrical properties of the subsurface. A detailed comparison of TDIP and FDIP methods, with a particular emphasis on the spectral content can be found in the studies by Flores Orozco et al. [27], Maurya et al. [53], and Martin et al. [52]. For a comprehensive introduction into the SIP method we refer to Sumner [73] and Binley and Slater [7].

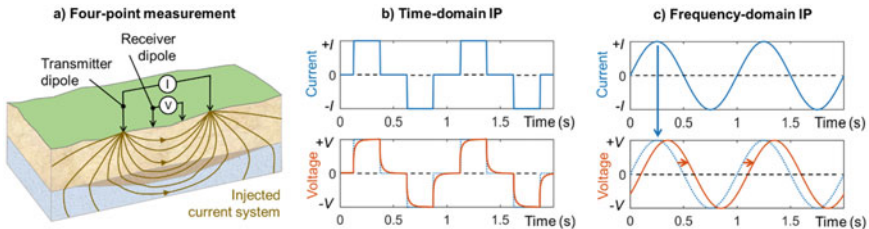


Fig. 15.1 Induced polarization (IP) measurement setup and wave forms. **a** Four-point measurement including a transmitter dipole for current injection, and a receiver dipole for voltage measurement. The distribution of the electrical current depends on the electrical resistivity of the subsurface materials. **b** For time-domain (TDIP) measurements, a square wave signal is injected into the ground; depending on the capacitive properties, the transient voltage signal is related to the charging and de-charging of the subsurface materials. **c** In frequency domain, (FDIP) these capacitive properties lead to a phase shift between alternating current and voltage signals

SIP imaging data are collected using tens to hundreds of electrodes and usually comprise hundreds to thousands of individual quadrupole (4-electrode) measurements. By varying the position of such quadrupoles along a line or surface, information on the lateral variation of electrical properties is gained. The total size of the electrode array, together with the electrical properties of the subsurface, control the depth of investigation of the measurement. In general, larger layouts gain information from deeper areas, while measurements with small separations between electrodes increase the resolution of near-surface data. However, conductive materials may channel the current flow limiting the sensitivity of the method to deeper areas. In order to reconstruct SIP images, measured transfer resistance and phase data are interpreted using inversion algorithms, which compute 2D sections—or 3D volumes—revealing the spatial variation of the electrical properties in the subsurface.

Here, we will limit ourselves to the discussion of results computed with smoothness-constraint inversion algorithms. This widely used inversion strategy favors the generation of electrical images with rather smooth transitions between regions of contrasting electrical properties. Kemna [44] and Binley and Slater [7] provide a revision on the inversion of TDIP and FDIP measurements. The open-source algorithms provided by Rücker et al. [63] and Johnson and Thomle [8] place well-established codes for the inversion of TDIP, FDIP and SIP datasets to the disposal of a broad audience. These algorithms have been used for the characterization of contaminated sites or the monitoring of groundwater remediation measures and permit using different inversion strategies, for instance, a frequency regularization to enhance the consistency of SIP imaging results at different frequencies [37, 41], a spatio-temporal regularization scheme for the inversion of monitoring data sets [21, 42, 46], or the use of a-priori information, such as structural constraints, to evaluate the performance of permeable reactive barriers of known geometry [70].

15.2 Electrical Properties of Natural Media

In the subsurface, electrical currents are mainly carried by the motion of ions through the electrolytic pore fluid. While most solid constituents of geologic materials can be considered electrically insulating (except for some metallic and other rare, conducting minerals), the mineral-electrolyte interface is covered by a conductive electrical double layer (EDL). The EDL (see Fig. 15.2a) forms due to the usually negative surface charge of the mineral and consists of two sections, (i) the Stern or fixed layer of counter-ions (cations) absorbed to the grain surface and (ii) the diffuse layer characterized by an increased concentration of counter-ions (cations) and a reduced concentration of co-ions (anions) compared to the undisturbed electrolyte. Driven by the electrical field imposed by the measuring device, ions in the electrolyte migrate along interconnected pathways in the water-filled pore space and ions in the EDL along interconnected surfaces (Fig. 15.2b). The amount of charges transported by these two conduction mechanisms known as electrolytic and surface conduction, respectively, controls the electrical conductivity (σ) of soils and rocks. In geophysics,

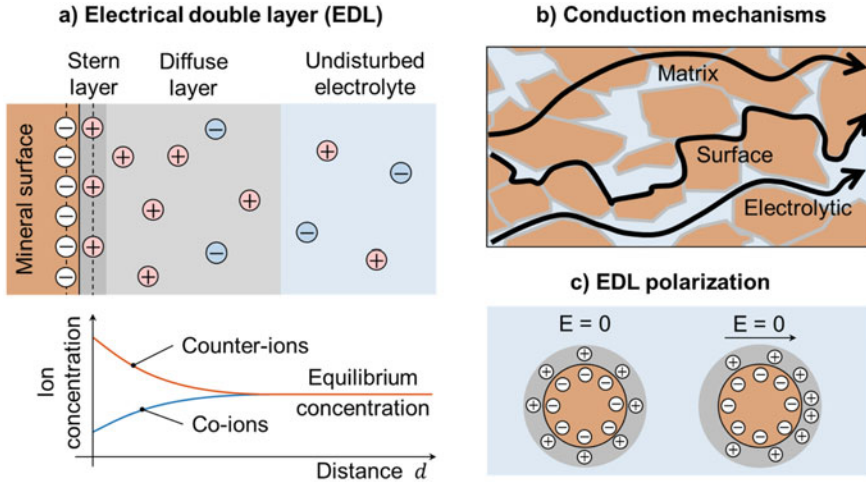


Fig. 15.2 Electrical properties of the mineral-electrolyte interface. **a** The usually negatively charged mineral surface is covered by an electrical double layer (EDL) consisting of the inner Stern and the outer diffuse layer. Across the diffuse layer, ion concentrations transition from their perturbed values at the mineral surface into the equilibrium concentration in the electrolyte. **b** Electrical conduction mechanisms including matrix conduction (often negligible), surface conduction, and electrolytic conduction. **c** Schematic sketch of the polarization of the EDL around a spherical grain: The application of an external electrical field leads to a redistribution of charges along the surface, the EDL polarizes

this property is often expressed in terms of the electrical resistivity $\rho = \sigma^{-1}$, the inverse of conductivity. Materials with highly charged surfaces and a large internal surface area, such as clay, often stand out with a high electrical conductivity (low resistivity). For further details we refer to Revil and Florsch [60], Kemna et al. [45], Bückler and Hördt [13], Bückler et al. [12].

Besides a considerable increase in conductivity, the EDL gives rise to the chargeability assessed by TDIP or the phase shift assessed by FDIP measurements. Driven by the external electrical field, the ions of the EDL accumulate on one side of the mineral grain and deplete at the other side. As soon as the external field is switched off (when the current injection is interrupted), diffusion forces redistribute the polarized charges within the EDL. This polarization and its relaxation result in the secondary voltage observed in TDIP or the phase shift in FDIP. As they do not only provide information about the conduction of current (i.e., migration of charges), but also information about the capacity of the subsurface to store charges (i.e., polarization of the EDL), IP methods offer additional complementary information compared to the resistivity method alone.

The bulk electrical conductivity of most natural media (except for metallic minerals or graphite) strongly depends on the conductivity of the pore fluid (σ_f). The porosity (θ , the ratio of pore volume to total volume) and the water saturation (S , the ratio of the water-saturated pore volume to the total pore volume) play

also an important role. Based on measurements on a large number of samples, [4] proposed an empirical model establishing a relation between these properties and the bulk conductivity of a material, which is widely used for hydrogeological and environmental investigations:

$$\sigma_{el} = \theta^m S^n \sigma_f$$

In this equation, also known as Archie's law, m and n are the cementation factor and the saturation exponent, respectively. The first is related to the connectivity between pores, while the second quantifies changes in the conductivity when replacing pore water by a non-conducting or fluid or gas. Both exponents are fitting parameters that need to be experimentally determined for each type of material. Since it has been established, many investigations have demonstrated the applicability of Archie's law to a wide range of rock and soil samples, as well as for different temperatures and chemical compositions of the pore water (see Glover [35]; and references therein). Nonetheless, in its original form, Archie's law does not hold for materials characterized by a large internal surface area and highly charged surfaces, such as clays, microbial cells, nanoparticles, organic matter, and in some cases contaminants. In these materials, surface conduction (σ_s) along the EDL plays a dominant role, which is not taken into account in Archie's law. Moreover, as discussed above, charges in the EDL polarize, which causes a frequency dependence of the electrical conductivity. To take both surface conduction and the associated polarization of charges into account, Archie's law can be expanded by adding a complex frequency-dependent surface conductivity $\sigma_s^*(\omega)$:

$$\sigma^*(\omega) = \theta^m S^n \sigma_f + \sigma_s^*(\omega)$$

Here, $\omega = 2\pi f$ is the angular frequency (in rad/s) associated to the frequency (f , in Hz) of the measurement. Complex-valued conductivities are convenient to calculate amplitude and phase of an alternating current together: The complex-valued surface conductivity σ_s^* , for instance, can be expressed in terms of its real component (σ_s'), which mostly describes Ohmic conduction or charge motion in-phase with the driving voltage, and its imaginary component (σ_s''), which quantifies the polarization properties or out-of-phase charge motion. By substituting $\sigma_s^* = \sigma_s' + i\sigma_s''$, where $i = \sqrt{-1}$, into the equation above, we can split the bulk conductivity of a material into a real part (σ') and an imaginary part (σ''):

$$\sigma^*(\omega) = \sigma' + i\sigma'' = [\sigma_{el} + \sigma_s'(\omega)] + i\sigma_s''(\omega),$$

Note that the real component contains contributions of electrolytic and surface conductivity, while the polarization is only related to the surface conductivity (σ_s'').

The SIP response of materials with one dominant polarization mechanism and a well-defined relaxation time scale (i.e., the time needed to establish the polarization of the material) is characterized by a well-pronounced peak in the phase (or imaginary conductivity) spectrum and an increase in the magnitude (or real conductivity). Such

a behavior can often be approximated by fitting relaxation models. One of the most widely used models for this purpose is the Cole–Cole model, which in terms of complex conductivity can be written as [57]:

$$\sigma^*(\omega) = \sigma_0 \left[1 + \frac{m(i\omega\tau)^c}{1 + (i\omega\tau)^c(1 - m)} \right] = \frac{1}{\rho^*(\omega)}$$

Here, σ_0 denotes the electrical conductivity at the low-frequency limit; m is the chargeability (between 0 and 1), which quantifies the amplitude of the polarization effect; $\tau = (2\pi f_c)^{-1}$ is the relaxation time, which is inversely proportional to the critical frequency (f_c), where the polarization peak is observed, and roughly proportional to the characteristic length scale of the polarization (e.g., the grain size or other important textural parameters); and c is a dispersion constant, which controls the broadness of the relaxation peak and roughly reflects the distribution of relevant relaxation times. The use of such relaxation models allows to reduce the rich information contained in highly resolved SIP data to a smaller number of relevant parameters. For further details, we refer the reader to Pelton et al. [57], Binley and Slater [7].

15.3 Electrical Properties of Contaminated Soil

Contaminants miscible in groundwater commonly tend to increase the real component of the electrical conductivity. Hence, geophysical electrical methods such as the electrical resistivity tomography (ERT), have been widely used in the last years for site characterization. For instance, conductive anomalies resolved through ERT have been used to image the leakage and migration of landfill leachates (e.g., De Carlo et al. [16]; Tsourlos et al. [74]; Soupios and Ntarlagiannis [71]; Nguyen et al. [55] and references therein). The accumulation of metallic ions or an increase in pH can also result in conductive anomalies; thus, ERT has been used to map heavy-metal contaminant plumes, acid mine drainage and other contaminants related to mine-tailings (e.g., Placencia-Gómez et al. [58]; Wang et al. [77]).

Hydrocarbon contaminants comprise a broad range of organic compounds such as chlorinated hydrocarbons (CHCs), polycyclic aromatic hydrocarbons (PAHs), aromatic hydrocarbons (e.g., the BTEX group: benzene, toluene, ethyl benzene and xylene), and phenols. These compounds are immiscible in water and represent some of the most important contaminants affecting soil and groundwater in Europe. Laboratory studies have demonstrated that fresh hydrocarbon contaminants effectively behave like electric insulators and that increasing their volumetric content in soils results in an increase of the electrical resistivity [17]. Hence, initial field studies demonstrated the applicability of the ERT method to delineate the geometry of fresh hydrocarbon-contaminant spills based on the detected resistive anomalies [6, 43, 64].

Like every indirect method, ERT methods suffer from the ambiguity in the interpretation of the resistivity values alone. IP or SIP methods for site characterization

respond to the necessity to gain further information and thereby reduce ambiguities in the interpretation. E.g., a conductive anomaly could either represent dissolved contaminants (e.g., landfill leachates) or simply reflect an elevated clay content in the host rock; resistive anomalies may indicate a fresh hydrocarbon spill or simply be related to unsaturated material or tight consolidated rock. By additionally analyzing the capacitive properties of the subsurface, or the induced polarization effect, the responses associated with the geology and those of the contaminants can often be discriminated better.

Especially in the case of hydrocarbon contaminants, various studies have revealed the sensitivity of SIP measurements to both chemical changes in the impacted groundwater and the geometry of the remaining water-filled pore space. The displacement of pore water by hydrocarbon contaminants modifies the geometry of the water-filled pore space and thus, the frequency dependence of the complex conductivity. These geometrical changes often result in a variation of the relaxation time (τ), which is known to be sensitive to the textural parameters of the material [45, 60]. Furthermore, hydrocarbons are organic compounds and as such may modify the chemical properties of the grain surfaces and thus the electrical properties of the EDL, which control the polarization response.

Olhoeft [56] carried out the first SIP measurements on soil samples impacted by organic waste and petroleum. His study revealed an increase in the conductivity phase (ϕ), which he attributed to interactions between the organic compounds and the surfaces of the solid constituent of the soil. This observation has prompted a large number of follow-up investigations over the last three decades, where the SIP response of a variety of organic compounds has been further evaluated in laboratory experiments. In summary, these investigations revealed that the polarity of the organic compounds as well as the hydrocarbon saturation mainly control the measured SIP response.

15.3.1 Hydrocarbons in Soils: Polar and Non-polar Compounds and Their SIP Response

Hydrocarbon contaminants are non-aqueous phase liquids (NAPL) that are—for practical reasons—classified into light NAPLs (or LNAPLs), which are less dense than water and float on the groundwater table, and dense NAPLs (DNAPLs), which are denser than water and sink down within the aquifer. In terms of electrical properties, the polarity of an organic contaminant, defined by its molecular electrostatic potential, is much more relevant than its density. “Non-polar” hydrocarbons form isolated droplets within the water filled pores because they lack ionic or polar groups to be attracted by the surrounding mineral surfaces (see Fig. 15.3a). They are also referred to as “non-wetting” hydrocarbons, considering that the pore water is in direct contact with the grain surface (i.e. water is the fluid wetting the grains). In contrast, “wetting” hydrocarbons do contain polar compounds and readily attach to the grain

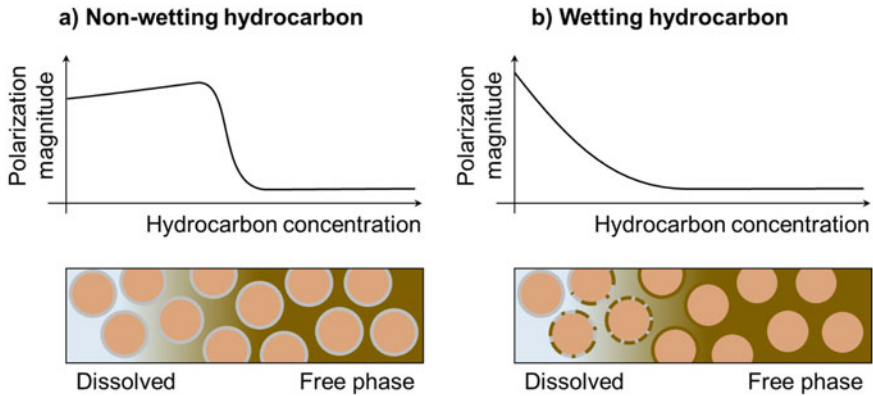


Fig. 15.3 Schematic sketch of the variation of the polarization magnitude with the contaminant concentration for **a** non-wetting and **b** wetting hydrocarbons

surfaces (see Fig. 15.3b), i.e., the liquid hydrocarbon is in direct contact with the grains. In this context, the wettability refers to the affinity of a specific NAPL for the soil surface [2].

In laboratory measurements, Schmutz et al. [65] observed a decrease of both real and imaginary conductivity (σ' and σ'') with increasing volumetric content of non-wetting hydrocarbon (see Fig. 15.3a). At the same time, the phase ($\phi \approx \sigma''/\sigma'$) increased with increasing volumetric content of non-wetting hydrocarbon. The critical frequency of the polarization (frequency at which the peak is observed) was found at low frequencies between 1 mHz and 1 Hz. In a similar study with non-wetting oils (e.g., paraffin and sunflower oil), Schmutz et al. [66] found contradictory trends, while Ustra et al. [75] also reported a negligible polarization in the low frequencies in columns experiments with toluene. Revil et al. [61] extended these experiments to investigate wetting oils and observed a decrease in ϕ as well as an increase in σ' with increasing oil volumetric content (see Fig. 15.3b). These results suggest that the introduction of a wetting oil, which—partly or entirely—covers the soil mineral surface, facilitates ion migration (increase of σ') rather than the accumulation and polarization of charges (decrease of ϕ). Schwartz et al. [67] and Schwartz and Furman [68] argue that the decrease in the polarization magnitude is a consequence of the adsorption of organic molecules to the mineral surface and the release of inorganic ions to the bulk electrolyte, resulting in an increase in σ' , and a decrease in both parameters expressing the polarization effect (ϕ and σ'').

Bucker et al. [10] recently proposed a mechanistic model to understand the SIP response of wetting and non-wetting hydrocarbon contaminants. Based on a membrane polarization model [13], they do not only take the hydrocarbon concentration into account, but also the surface charge at the hydrocarbon-water interface, as well as the geometrical configuration of water and hydrocarbon. They predict a decrease of σ' and ϕ with increasing hydrocarbon saturation irrespective of whether the hydrocarbon is wetting or non-wetting. Non-wetting hydrocarbons

with highly charged surfaces yield an increase of the conductivity magnitude with hydrocarbon saturation and a slight increase of the phase at intermediate hydrocarbon concentrations as sketched in Fig. 15.3a.

15.3.2 *Electrical Properties of Mature Hydrocarbon Plumes*

While pure hydrocarbons behave as electrical insulators, many studies on aged hydrocarbon-contaminated soil and rock materials have revealed high electrical conductivity values. This apparent contradiction has been resolved by attributing the increased conductivity to the effect of biotic and abiotic transformations of the contaminants and the accumulation of metabolic products in the pore water (e.g., Atekwana and Atekwana [5]; and references therein).

Hydrocarbons are electron donors and can be degraded by different bacterial strains [19, 33, 34]. This biodegradation depends on the adaptation of microorganisms to available electron acceptors and the respective energy yield. Differences in the energy efficiency of aerobic and anaerobic respiration and the successive depletion of electron acceptors leads to a sequence of redox reactions: After the oxygen is consumed by oxidizing bacteria (aerobic respiration), nitrate-reducing or denitrifying bacteria are responsible for the most effective anaerobic respiration, followed by manganese and iron reducing bacteria; and lastly sulfate-reducing microorganism. In absence of inorganic electron acceptors besides carbon dioxide (CO₂), methanogenesis, as a last step in the sequence of redox reaction, still permits the degradation of a variety of hydrocarbon contaminants [34, 47, 51]. Flores Orozco [32] and Flores Orozco et al. [31] have shown the sensitivity of the SIP imaging method to variations in the redox-status of the subsurface, thus, its potential to delineate redox zonation in contaminant plumes.

Besides the transformation of the hydrocarbon contaminant, the microbial activity results in the accumulation of metabolic products, such as carbonic acids, dissolved nitrate, iron or manganese in the surrounding groundwater, which in turn may result in the precipitation of minerals such as iron sulfides (e.g., Mewafy et al. [54]). Henceforth, the term “mature” plume refers to contaminant plumes undergoing such a biogeochemical transformation. The time required to reach such maturity depends on the availability of indigenous microorganisms and electron acceptors and varies largely between sites.

As stated above, the release of metabolic products often results in an increase of pore-water salinity around mature plumes and explains the conductive anomalies observed in ERT images (e.g., Atekwana and Atekwana [5]). An increasing pore-water salinity may also increase the polarization response (σ'') in SIP surveys, (e.g., Revil and Skold [62]; Hördt et al. [39]). However, laboratory studies indicate that this increase is only observed up to a certain salinity threshold and that σ'' values decrease at even higher ionic concentrations (e.g., Weller et al. [78]; Hördt et al. [39]). Based on their membrane polarization model, Hördt et al. [39] attribute this

maximum behavior to the salinity-dependent variation of the double-layer thickness at the mineral surface.

The stimulation of microbial activity by contaminants as carbon source also results in the accumulation of microbial cells and the formation of biofilms. Thus, the observed increase in both σ' and σ'' in mature plumes has also been attributed to the electrical properties of microbial cells, which have a surface area and a surface charge similar to clay minerals [3], or the weathering of grains, which is enhanced by the release of carbonic acids during microbially mediated reactions [1]. Recent studies suggest that the precipitation of electrically conducting minerals, such as iron-sulfides, following the activity of iron- and sulfate-reducing bacteria could explain the observed increase in both components of the complex conductivity σ^* [2, 54]. Electrical conductors permit the flow of current through electronic conduction (i.e., by the movement of electrons), which is often related to much higher conductivities than in the case of electrolytic and even surface conduction. Accordingly, the charges on the electrical conductor also polarize and increase the SIP response. For more details on this so-called electrode -polarization, see Bucker et al. [11, 14] and Revil et al. [59].

The vast number of laboratory data and accompanying modeling studies discussed above indicates a high sensitivity of the SIP method to both changes in the chemical composition of the pore water and changes in the pore-space geometry. Based on these findings, the SIP method appears to be a promising technique for site characterization and the monitoring of contaminant transformation. However, to date, only few studies investigate the SIP response at the field scale in detail. To fill this gap, in the following sections, we present SIP field data and show that the obtained imaging results clearly indicate the method's suitability for the characterization of a range of different hydrocarbon contaminants even under real-world field conditions.

15.4 Field Procedure and Data Processing

As noted above, laboratory studies indicate that hydrocarbon contaminants can cause significant contrasts with respect to electrical conductivity and polarization properties of the subsurface. However, to date only few studies have addressed the actual frequency dependence of the electrical response of hydrocarbon plumes in the field. The application of the SIP method at the field scale faces multiple challenges including instrumentation and survey design, data processing and inversion, as well as the interpretation of the imaging results.

In order to illustrate these challenges, we present exemplary raw data and imaging results of a SIP survey conducted on the grounds of a former hydrogenation plant, where groundwater is impacted by high concentrations of benzene. Benzene is a non-polar and non-wetting hydrocarbon with a saturation concentration of 1.79 g/L (at 15 °C). The lithology at the study site consists of three layers (from top to bottom): (1) backfill material with a thickness of approx. 2 m, (2) a sandy to gravelly unit with a thickness of approx. 9 m hosting the aquifer, and (3) a layer of clay and lignite, which

limits the aquifer downwards. During the survey, the groundwater table was located at a depth of -8 m. The SIP profile was centered at the zone, where high benzene concentrations > 2.2 g/L in groundwater indicated free-phase benzene. Contaminant concentrations decreased towards both ends of the profile.

To minimize the distortion of readings by anthropogenic noise due to pipes, storage tanks, power lines, or other subsurface installations, the SIP survey was conducted on the bottom of a trench, after the removal of the backfill material. 37 stainless steel electrodes were installed with a unit electrode spacing of 2.5 m (resulting in a total profile length of 90 m). The electrical impedance measurements were collected with a SIP256C (from Radic Research), using an actual sinusoidal waveform at 15 logarithmically equidistant frequencies between 0.07 and 1,000 Hz. The electrode configuration was a dipole–dipole “skip-3”, which means that the separated current and potential dipoles had a length of 4 times the unit electrode spacing (3 electrodes skipped between the poles).

One of the challenges regarding spatially resolved SIP field measurements is related to the adverse effect of polarized electrodes: The circulation of a current flow through a grounded electrode results in redox reactions at the surface of the metallic bar that might result in a remnant polarization affecting the quality of subsequent voltage readings [18, 48, 79]. Here, this issue was resolved by designing the dipole–dipole measuring protocol in such way that voltage measurements with electrodes, which have previously been used for current injection, were excluded. In other words, the voltage measurements were always collected with electrodes ahead of the current dipole.

Figure 15.4 shows the frequency dependence of the SIP raw data in terms of apparent conductivity magnitude (σ_{app}) and phase (ϕ_{app}). The apparent conductivity magnitude is computed from the measured impedance magnitude as $\sigma_{app} = (|Z|k)^{-1}$, where the geometrical factor k accounts for the geometrical configuration of the electrode layout; ϕ_{app} is equal to the measured phase. These apparent quantities do not represent a true image of the spatial variation of the electrical conductivity in the subsurface, which can only be obtained after the inversion of the data. However, they do permit a first visualization and assessment of the overall response including the frequency dependence of the electrical properties. The frequency dependence of the apparent conductivity of selected quadrupoles along the SIP profile in Fig. 15.4 (last row) shows different behaviors, which can roughly be attributed to three units: (1) the unsaturated soils on the top assessed by shallow measurements (center of the profile, short separation between current and potential dipole); (2) the free-phase contaminant or source zone (center of the profile, intermediate dipole separation); and (3) the plume of dissolved contaminants (first and last dipoles of the profile, intermediate dipole separations).

The steep increase of the phase values at frequencies > 100 Hz evidences another challenge of SIP data acquisition in the field: In small-scale (i.e., cm to dm range) laboratory data, a similar increase is often related to Maxwell–Wagner polarization processes (e.g., Revil et al. [61]), which reflect the polarization of interfaces between two or more materials of varying conductivity but may not be confused with polarization processes in the EDL, which are observed at lower frequencies. In contrast,

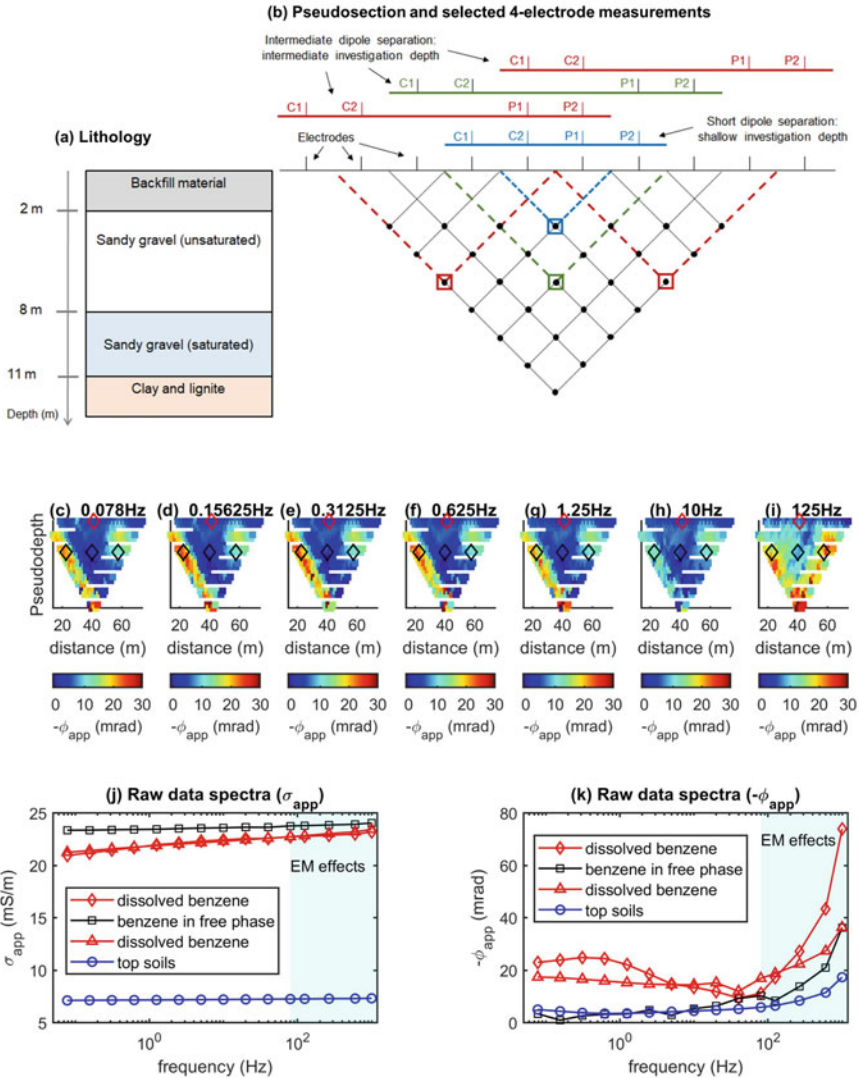


Fig. 15.4 SIP raw data collected over a benzene plume. **a** Lithology of the study area and **b** Schematic representation of a pseudo section including the selected pixels for the analysis of the raw data spectra. **c** to **i** pseudo sections representing the measured impedance phase values (ϕ_{app}), with the diamonds indicating the selected quadrupoles for the analysis of the raw data spectra. Raw data spectra for the selected quadrupoles expressed in terms of **j** the magnitude of the apparent conductivity (σ_{app}) and **k** the apparent phase (ϕ_{app}). The steep increase of ϕ_{app} at high frequencies indicates electromagnetic (EM) coupling effects.

high-frequency SIP measurements collected with large electrode layouts as usually used in the field (10 to 100 s of meters) are mainly affected by electromagnetic (EM) coupling, which comprises both inductive and capacitive effects along the cables connecting the measuring instrument with the electrodes. Phase readings affected by inductive EM-coupling increase linearly with acquisition frequency, ground conductivity and the square of the cable length [23, 24]. Hence, inductive coupling likely becomes important in the case of mature plumes, due to the expected increase in the bulk electrical conductivity, as discussed above.

Sometimes, EM-coupling is argued to be negligible at frequencies < 10 Hz (e.g., Kemna et al. [45]). However, unshielded multicore cables, such as those typically used for resistivity surveys, may provoke significant EM coupling in SIP data even at frequencies as low as 1 Hz. Therefore, Flores Orozco et al. [23] recently recommended the use of shielded cables to minimize inductive coupling due to cross talking between cables, and to improve the overall quality of SIP readings. The SIP256C measurement device used in this field-data example follows an alternative approach: Voltage readings are digitized directly at the electrode, which largely reduces cross talking between cables (e.g., Martin et al. [52]). Even though, the steep increase of ϕ_{app} at frequencies > 100 Hz (Fig. 15.4k) is a clear indication of a significant EM coupling. Besides adjustments to the instrumentation, different techniques have been suggested for the de-coupling of the data during processing (e.g., Pelton et al. [57]). Because their applicability is limited and taking into account that laboratory experiments have mainly revealed a significant frequency dependence in hydrocarbon-impacted sediments below 10 Hz, we hereafter only discuss the results collected at frequencies < 200 Hz.

The pseudo sections in Fig. 15.4 are constructed by plotting the values of ϕ_{app} below the midpoint of the respective quadrupoles and at “pseudo” depths, which are proportional to the total quadrupole length (or dipole separation). Considering that subsequent quadrupole readings along the profile measure overlapping volumes of the subsurface, pseudo sections are expected to vary gradually in both lateral and vertical direction. Thus, abrupt changes between neighboring points of the pseudo section indicate outliers or erroneous measurements (see Flores Orozco et al. [23]). Such outliers and erroneous measurements need to be removed before the inversion, otherwise structures in the resulting images may be generated that are only related to noise in the data and not to subsurface properties (also referred to as inversion artifacts). The pseudo sections in Fig. 15.4 vary smoothly at all frequencies. A slightly increased variability in the values is observed at large pseudo depths, corresponding to readings with large separations between current and potential dipole, which are affected by a poor signal-to-noise (S/N) ratio.

The above analysis of the pseudo-section visualizations permits a qualitative identification of outliers and erroneous measurements, but strongly depends on the experience of the user. A more quantitative approach is based on the analysis of the difference between normal and reciprocal readings. Here, reciprocal readings refer to measurements of the same quadrupole but with interchanged current and voltage dipoles. Initially proposed for ERT measurements by LaBrecque et al. [49], this method is based on the principle of reciprocity, which states that (theoretically)

normal and reciprocal measurements should be identical. Thus, a statistical analysis of the normal-reciprocal misfit can be used to quantify random error in the data. The occurrence of large misfits between normal and reciprocal readings is also useful to identify outliers or systematic sources of error, which might e.g. be related to a poor galvanic contact of the electrodes with the ground. The applicability of the normal-reciprocal analysis to FDIP and TDIP data has been documented in various studies (e.g., Slater and Binley [70]; Flores Orozco et al. [24, 28]). However, the collection of reciprocals at all frequencies of a SIP survey would be challenging considering that measurements at frequencies <5 Hz are related to long acquisition times. Hence, we recommend to collect reciprocals down to at least at 1 Hz and use the analysis of normal-reciprocal misfits to establish thresholds values (for injected current, voltage, and ϕ_{app}) that permits filtering of the low-frequency data, in case that the collection of reciprocals is not possible due to time constraints. The collection of reciprocals at high frequencies is also recommended to discriminate between EM coupling and other sources of error.

In the present case, the analysis of the normal–reciprocal misfit was conducted at all frequencies individually resulting in relative and absolute errors of 5% and 1 Ω , respectively, for the impedance magnitude and a constant absolute error of 5 mrad for the impedance phase. Independent inversions of single-frequency data converged to a weighted root mean square error (RMSE) of 1.0 ± 0.05 , meaning that the obtained model explains the data within these error bounds.

Independently from the chosen approach, the use of a consistent (and ideally quantitative) methodology for the processing of the data is critical to warrant the comparability of inversion results for data collected at different frequencies (e.g., Flores Orozco et al. [24, 31]). Furthermore, poor processing might lead to the creation of inversion artifacts. Accordingly, an inadequate identification of erroneous measurements and outliers might have a large influence in the inverted imaging results; thus, leading to an inadequate site characterization and hindering a more detailed analysis of the frequency dependence.

Instead of carefully processing the raw data, the consistency between inversion results obtained at different frequencies can also be enforced during the inversion. The use of spatial and frequency regularization schemes (e.g., Günther and Martin [37]) permits to impose an expected spectral response, such as a Cole–Cole relaxation, during the simultaneous inversion of data collected at different frequencies. However, an adequate processing of the raw data has been demonstrated to minimize the impacts of cultural noise in IP monitoring results [26] as well as to provide better results than the use of (multiple) regularizations (e.g., Lesparre et al. [50]).

15.5 Interpretation of Field-Scale SIP Imaging Results

The inversion results of SIP data collected along one measurement line consist of 2D sections revealing both lateral and vertical changes in the electrical properties of the subsurface. If data was collected along several parallel lines or with electrodes

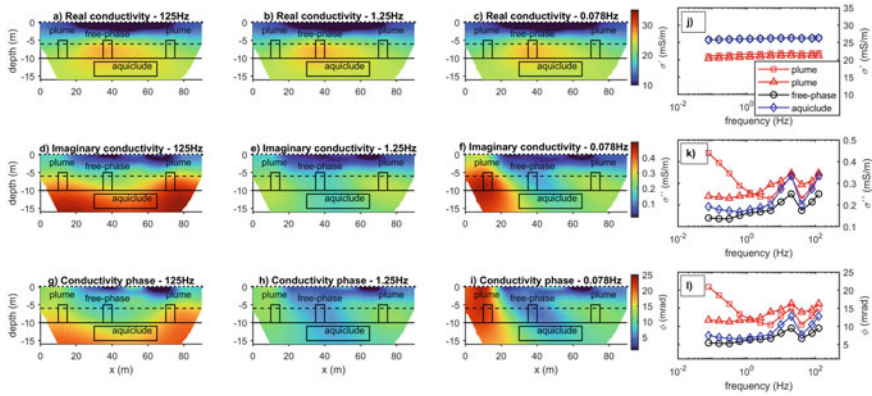


Fig. 15.5 SIP imaging results expressed in terms of the real (*a, b, c*) and imaginary (*d, e, f*) component of the complex conductivity (σ^*), as well as their ratio expressed by the phase ($\phi \approx \sigma''/\sigma'$) for data collected at two different frequencies (*g, h, i*). The spectral response of the electrical parameters (*j, k, l*) for selected areas, which are indicated by black boxes in the electrical images. The position of the electrodes along the surface (black circles), the groundwater level (dashed line), and the limit of the aquifer (solid line) are indicated, too

distributed over a grid, a 3D inversion can be carried out to obtain a 3D model of the subsurface. The results are usually expressed in terms of the complex resistivity (ρ^*) or its inverse, the electric conductivity (σ^*). In either case, the complex quantity can be visualized in terms of real and imaginary components, or as magnitude and phase. In Fig. 15.5, we present the imaging results of the data collected at the benzene-contaminated site in terms of real (σ') and imaginary (σ'') conductivity as well as conductivity phase (ϕ) at low (0.078 Hz) and high (125 Hz) frequencies, respectively. Because $\sigma' \gg \sigma''$ and thus $|\sigma^*| \approx \sigma'$, the magnitude image is practically equal to the real part image and not shown here for brevity.

The real part of electrical conductivity (σ') reveals two main units (Fig. 15.5a–c): (i) an uppermost layer with low conductivities (< 10 mS/m) associated with the unsaturated soils and (ii) a second, more conductive layer, which extends from 7.5 m downward and corresponds to the saturated sediments of the aquifer. A highly conductive anomaly (up to 25 mS/m) is located at the position of the benzene in free phase, i.e. the source zone, and corresponds with the expected signature of a mature plume undergoing degradation. The known lithological contact with the clay-rich formation at 11 m depth is not easily identified at both ends of the geoelectrical section, but may be inferred from the maximum depth of the conductive anomaly at its center. As expected from the flat frequency response of the σ_{app} raw data, no significant differences exist between low and high frequency σ' images. As discussed above, the high values in σ' are likely related to the accumulation of metabolic products, which increase the salinity and thus the electrolytic conductivity of the pore water.

The polarization properties of the subsurface are expressed in terms of both the imaginary conductivity σ'' (Fig. 15.5d–f) and the conductivity phase ϕ (Fig. 15.5g–i) to permit a direct comparison with laboratory results (e.g., Schmutz et al. [61]; Revil

et al. [65]). The σ'' and ϕ images clearly reveal contrasts between unsaturated and saturated materials as well as between the benzene in the dissolved plume and in free phase. The lowest polarization response is observed at the center of the section within the saturated zone, where high contaminant concentrations indicate the presence of free-phase benzene. At the same time, σ'' and ϕ values in the plume first increase with the distance to the source area and then slightly decrease towards both ends of the profile.

Similar observations, i.e., a slight increase of the polarization response with increasing contaminant concentration in the plume and a largely reduced polarization within the source area, have been reported earlier by Flores Orozco et al. [27] from a BTEX-contaminated site. Bucker et al. [10] attributed this behavior to the geometrical configuration of the contaminant within the pore space. In their model, the polarization response of non-wetting hydrocarbons increases with increasing concentration but strongly decreases as soon as the contaminant droplets of neighboring pores become continuous across the connecting pore throats.

Besides the clear response of free-phase benzene and the associated plume at intermediate depths, there are two more features of the polarization images (i.e., σ'' and ϕ), which are worth mentioning. Firstly, the uppermost layer (first 2 m) shows large heterogeneities with respect to both σ'' and ϕ , which are likely related to anthropogenic structures still in place after the removal of the backfill material. Secondly, the high-frequency images show a strong increase below 5–10 m depth, which most likely reflects the strong polarization response of the clayey formation confining the aquifer at depth, due to polarization of the Stern layer or membrane polarization mechanisms (e.g., Revil and Florsch [60]; Bucker et al. [26]).

As expected from the flat frequency response of the σ_{app} raw data, the spectral variation of σ' is weak within all three zones of interest (see Fig. 15.5j). At the same time, the spectral variation of σ'' and ϕ (see Fig. 15.5k and l) of free-phase benzene (source zone), plume and aquiclude are readily distinguished: Particularly the increase of both parameters at low frequencies (<1 Hz) seems to be characteristic for the plume of dissolved benzene, while the response is much lower and eventually flattens out in the source zone and aquiclude. It is worth mentioning that a similar behavior, i.e. an increase in the polarization with increasing benzene concentrations has also been observed in laboratory measurements on non-polar hydrocarbon compounds (e.g., Schmutz et al. [66, 65, 67]; Deceuster and Kaufman [20]; Shefer et al. [69]; Blondel et al. [9])

At intermediate frequencies (at 2 Hz) a phase peak appears in all four spectra (Fig. 15.5k and l), which we therefore interpret as the characteristic response of the background material. Most probably, this peak is related to the fine-grained fraction as it is most pronounced within the clayey aquiclude and weaker within the sandy to gravely aquifer. At higher frequencies, the response is increasingly affected by EM coupling, which makes the interpretation difficult.

A comparison of the apparent electrical conductivity in Fig. 15.4 with the inverted complex conductivity image in Fig. 15.5 reveals that the general trends regarding the frequency dependence of the electrical parameters are visible in both data and inverted model parameters. This is particularly important, as in the approach chosen here, the

inversions are carried out independently for each frequency and no regularization is used to enforce spectral consistency of the inverted models.

While the results presented here are based on a multi-frequency measurement, recent investigations propose to retrieve the spectral variation of $\sigma^*(\omega)$ from full-wave form TDIP data (e.g., Fiandaca et al. [22]). This approach also improves the investigation of contaminated sites compared to a pure ERT survey or the use of integral chargeability values [40, 53]. However, the TDIP data is fitted to a relaxation model, the selection of which strongly predetermines the possible frequency dependencies of $\sigma^*(\omega)$. As the present case study illustrates, properties such as chemical composition of groundwater (here, contaminant concentration and fluid conductivity), biogeochemical processes as well as the pore-space geometry have a large and likely site-specific influence on the electrical response. In particular, the complex interplay of these properties may result in spectral responses consisting of multiple relaxations, the recovery of which might be challenging for full-wave form inversion approaches. Therefore, we stress that the collection of SIP data in the frequency domain is the most direct way to evaluate the frequency dependence of the electrical properties of subsurface materials.

Flores Orozco et al. [25] demonstrated the use of coaxial cables to collect high quality SIP data in a site impacted by a jet fuel spill. The results in that study are consistent to those presented in Fig. 15.5. In their study, Flores Orozco et al. [25] also reveal variation in the frequency dependence of the complex conductivity in imaging data sets collected in clean sediments, the plume of dissolved contaminants and close to the source zone, where free-phase oil is trapped within the pore space. The interpretation of SIP results was confirmed through laser induced fluorescence (LIF) loggings. Clearly the analysis of the frequency-dependence in the polarization response provides an improved site characterization than those investigations conducted solely with DC-resistivity methods, or single-frequency IP.

15.6 Monitoring of Nanoparticles Injections for Groundwater Remediation

To illustrate the applicability of the IP method as a monitoring tool, e.g., to accompany the application of remediation measures, we present here imaging results obtained along the injection of micro-scale iron particles. The measurements were collected inside an industrial area, where groundwater is impacted by chlorinated aliphatic hydrocarbons (CAHs), especially TCE (chlorinated ethane) released during the production of solvent-based paints. TCE is polar hydrocarbon, which is denser than water (DNAPL). The injection of reactive nano- and micro-scale particles into the subsurface is a promising approach for the in-situ degradation of pollutants as it reduces remediation times and can be applied to areas not accessible by common remediation techniques (e.g., Grieger et al. [36] and references therein). A variety of techniques has been proposed for the remediation of CAH plumes, yet, it is beyond the

scope of this chapter to discuss these techniques and the accompanying changes in the electrical properties in detail. Nonetheless, the following case study demonstrates the sensitivity of the complex resistivity to different chemical processes as needed for an improved delineation of subsurface processes compared to the resistivity magnitude alone.

The study area can be described by three main units (from top to bottom): (1) a shallow aquifer comprised of gravel and sand with a thickness of ca. 4.5 m, (2) an aquiclude composed by clay-rich sediments (between 4.5 and 8 m depth), and (3) a deep aquifer composed of coarse sand and gravels. A schematic representation of the site is presented in Fig. 15.6a. The remediation targeted the deep aquifer, where guar-gum coated micro-scale zero-valent iron particles (GG-mZVI) [76] were injected between 10.5 and 8.5 m depth in 0.5 m steps, starting at the deepest position (see Fig. 15.6a). Each injection step had a duration of 15 min and aimed at delivering 20 kg mZVI at low pressures. During the injections it took another 15 min to relocate the pump and collect IP data.

IP measurements were collected during the relocation of the pump at a single frequency (1 Hz) using 24 stainless steel electrodes with a separation of 1 m. The profile was centered at the position of the injection well. For further details, we refer to Flores Orozco et al. [30]. Baseline imaging results obtained from data collected one day before the GG-mZVI injection reflect the known three-layered geology (Fig. 15.6a). A noticeable anomaly characterized by high σ^* values corresponds to

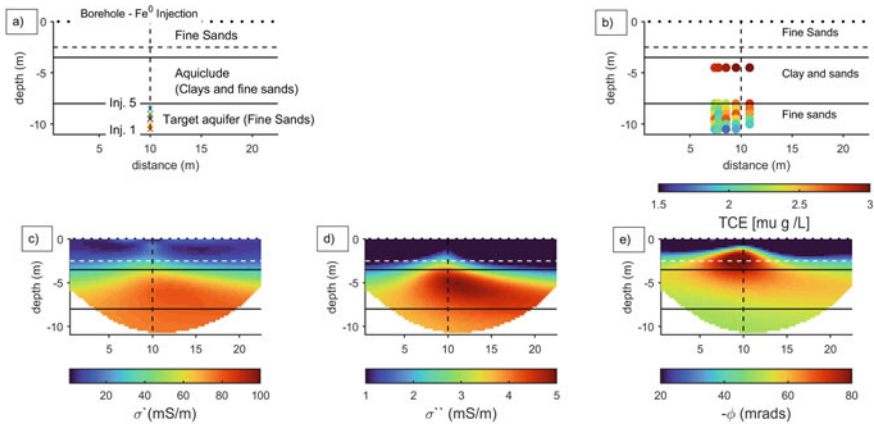


Fig. 15.6 Contaminant concentrations and imaging results for baseline measurements collected at a TCE-impacted site prior to the injection of guar-gum coated micro-scale zero-valent iron (GG-mZVI). **a** schematic representation of the lithological units at the site and the protocol used for the injection (Inj.) of the GG-mZVI, and **b** reported concentrations of TCE in groundwater samples collected before subsurface amendment. Complex conductivity imaging results expressed in terms of the real **c** and imaginary **d** components as well as the conductivity phase **e**. The horizontal solid lines indicate the position of the aquiclude, the dashed line indicates the depth of the groundwater table during the IP survey, and the black dots along the surface the electrode positions. Figure modified from [30]

the plume of dissolved TCE observed e.g., in Fig. 15.6b (concentrations in groundwater – 1 mg/L). The lack of information about TCE concentrations within the clay-sand aquitard is due to the practical limitations of direct site-investigation methods, for instance based on the extraction of groundwater samples, which cannot be carried out in low permeable formations. The increase in conductivity observed in Fig. 15.6c may again reflect the maturity of the organic contaminant. Besides, as a polar hydrocarbon, TCE might also result in highly charged surfaces of the hydrocarbon phase as modelled by Bückner et al. [10], explaining the increase in the polarization response. Similar responses have also been observed in TDIP investigations on other CAHs contaminated materials [15, 38, 40, 72].

The monitoring results presented in Fig. 15.7 reflect the absolute change between the baseline image and the images obtained after each injection step. Both conductivity magnitude and phase reveal an increase in the deep aquifer as the injection proceeds. This is the expected effect of the amendment of GG-mZVI, as the stabilizing solution is more conductive than the local groundwater and the coated iron particles are expected to cause a strong electrode-polarization response. Beside the changes in the deep aquifer, even larger changes (>50%) can be observed within the shallow sediments, a few meters above the injection points. These unexpected changes indicate the migration of particles along vertical flow paths. Such preferential flow paths are due to fractures created during the injection that resulted in an off-target delivery of the particles. Geochemical data obtained from the analysis of cores recovered after the injection confirmed the migration of particles and stabilizing solution to shallow areas through fractures. Additionally, properly delivered particles in the deep aquifer can be related to the positive changes in both IP images between 8 and 10 m depth. Likely due to the enzymatic consumption of the guar-gum coating upon the arrival in the targeted aquifer, the bare metallic particle develops a strong electrode polarization response. On the contrary, the particles delivered off-target in

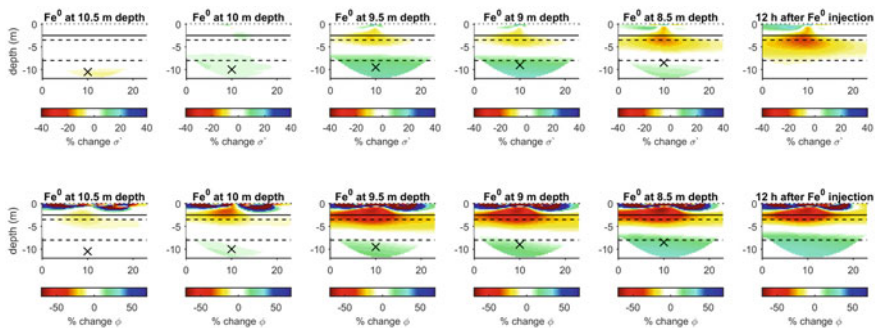


Fig. 15.7 Absolute temporal changes in the IP imaging results computed as the differences between baseline and time-lapse data after each particle injection. IP parameters are expressed in terms of conductivity magnitude (top) and phase (bottom). Spatial variations in the IP response are related to the accumulation of: bare particles in the deep aquifer close to the injection points (indicated by “x”) and coated GG-mZVI delivered off-target into the unsaturated zone. The dashed horizontal lines represent lithological contacts and the solid line the groundwater table

the unsaturated zone and shallow aquifer are still coated by the guar-gum; thus, the metallic surfaces are not in direct contact with the electrolyte, hindering the development of electrode polarization. A more detailed discussion can be found in Flores Orozco et al. [30]. Additionally, monitoring results obtained along the injection of nano-scale Goethite particles by Flores Orozco et al. [29] demonstrates the abilities of electrical monitoring to delineate clogging of the pore space following the injection of nano-Goethite particles, which in turn resulted in fracking and daylighting, i.e., particles flowing to the surface.

15.7 Summary and Conclusions

The two case studies illustrate that using the SIP method improves the characterization of contaminated sites compared to resistivity methods alone. While the conductivity magnitude (i.e., resistivity) is mainly sensitive to lithological changes and variations in the fluid conductivity, the polarization properties assessed by the SIP method are sensitive to the presence of immiscible fluids, such as hydrocarbon contaminants, to the resulting changes in the pore-space geometry, and the accumulation of metabolic products accompanying the natural transformation of organic contaminants. The polarization effect can be expressed in terms of both the imaginary component and the phase of the complex conductivity. Moreover, an analysis of the frequency dependence of these polarization properties can provide further information for the interpretation of the imaging results. In particular, we highlighted the possibility to measure comparable responses not only under well-controlled conditions in the laboratory but also in field-scale investigations. Even though the obtained results are promising, further field investigations are needed to fully understand the electrical response of contaminated subsurface materials. Despite the lack of a universal law linking contaminant concentration and electrical parameters, the SIP method can already be considered a practice-proven technique to delineate changes in the subsurface accompanying remediation techniques with a spatial and temporal resolution much higher than obtained with conventional sampling-based methods.

References

1. Aal GZA, Slater LD, Atekwana EA (2006) Induced-polarization measurements on unconsolidated sediments from a site of active hydrocarbon biodegradation. *Geophysics* 71(2):H13–H24
2. Abdel Aal GZ, Atekwana EA (2014) Spectral induced polarization (SIP) response of biodegraded oil in porous media. *Geophys J Int* 196(2):804–817
3. Abdel Aal GZ, Atekwana EA, Slater LD, Atekwana EA (2004) Effects of microbial processes on electrolytic and interfacial electrical properties of unconsolidated sediments. *Geophys Res Lett* 31(12)
4. Archie GE (1942) The electrical resistivity log as an aid in determining some reservoir characteristics. *Trans AIME* 146(01):54–62

5. Atekwana EA, Atekwana EA (2010) Geophysical signatures of microbial activity at hydrocarbon contaminated sites: a review. *Surv Geophys* 31:247–283
6. Benson AK, Payne KL, Stubben MA (1997) Mapping groundwater contamination using dc resistivity and VLF geophysical methods—a case study. *Geophysics* 62(1):80–86
7. Binley A, Slater L (2020) Resistivity and induced polarization: theory and applications to the near-surface earth. Cambridge University Press
8. Blanchy G, Saneiyani S, Boyd J, McLachlan P, Binley A (2020) ResIPy, an intuitive open source software for complex geoelectrical inversion/modeling. *Comput Geosci* 137:104423
9. Blondel A, Schmutz M, Franceschi M, Tichané F, Carles M (2014) Temporal evolution of the geoelectrical response on a hydrocarbon contaminated site. *J Appl Geophys* 103:161–171
10. Bucker M, Flores Orozco A, Hördt A, Kemna A (2017) An analytical membrane-polarization model to predict the complex conductivity signature of immiscible liquid hydrocarbon contaminants. *Near Surf Geophys* 15(6):547–562
11. Bucker M, Flores Orozco A, Kemna A (2018) Electrochemical polarization around metallic particles—Part 1: the role of diffuse-layer and volume-diffusion relaxation. *Geophysics* 83(4):E203–E217
12. Bucker M, Flores Orozco A, Undorf S, Kemna A (2019) On the role of stern-and diffuse-layer polarization mechanisms in porous media. *J Geophys Res: Solid Earth* 124(6):5656–5677
13. Bucker M, Hördt A (2013) Analytical modelling of membrane polarization with explicit parametrization of pore radii and the electrical double layer. *Geophys J Int* 194(2):804–813
14. Bucker M, Undorf S, Flores Orozco A, Kemna A (2019) Electrochemical polarization around metallic particles—Part 2: the role of diffuse surface charge. *Geophysics* 84(2):E57–E73
15. Cardarelli E, Di Filippo G (2009) Electrical resistivity and induced polarization tomography in identifying the plume of chlorinated hydrocarbons in sedimentary formation: a case study in Rho (Milan—Italy). *Waste Manage Res* 27(6):595–602
16. De Carlo L, Perri MT, Caputo MC, Deiana R, Vurro M, Cassiani G (2013) Characterization of a dismissed landfill via electrical resistivity tomography and mise-à-la-masse method. *J Appl Geophys* 98:1–10. <https://doi.org/10.1016/j.jappgeo.2013.07.010>
17. Cassiani G, Kemna A, Villa A, Zimmermann E (2009) Spectral induced polarization for the characterization of free-phase hydrocarbon contamination of sediments with low clay content. *Near Surf Geophys* 7(5–6):547–562
18. Dahlin T, Leroux V, Nissen J (2002) Measuring techniques in induced polarisation imaging. *J Appl Geophys* 50(3):279–298
19. Das N, Chandran P (2011) Microbial degradation of petroleum hydrocarbon contaminants: an overview. *Biotechnol Res Int*
20. Deceuster J, Kaufmann O (2012) Improving the delineation of hydrocarbon-impacted soils and water through induced polarization (IP) tomographies: a field study at an industrial waste land. *J Contam Hydrol* 136:25–42
21. Doetsch J, Ingeman-Nielsen T, Christiansen AV, Fiandaca G, Auken E, Elberling B (2015) Direct current (DC) resistivity and induced polarization (IP) monitoring of active layer dynamics at high temporal resolution. *Cold Reg Sci Technol* 119:16–28
22. Fiandaca G, Auken E, Christiansen AV, Gazoty A (2012) Full waveform modelling of time domain induced polarization. *Geophysics* 71:G43–G51
23. Flores Orozco A, Aigner L, Gallistl J (2021) Investigation of cable effects in spectral induced polarization imaging at the field scale using multicore and coaxial cables. *Geophysics* 86(1):E59–E75
24. Flores Orozco A, Bucker M, Steiner M, Malet JP (2018) Complex-conductivity imaging for the understanding of landslide architecture. *Eng Geol* 243:241–252
25. Flores Orozco A, Ciampi P, Katona T, Censini M, Papini MP, Deidda GP, Cassiani G (2021) Delineation of hydrocarbon contaminants with multi-frequency complex conductivity imaging. *Sci Total Environ* 768:144997
26. Flores Orozco A, Kemna A, Binley A, Cassiani G (2019) Analysis of time-lapse data error in complex conductivity imaging to alleviate anthropogenic noise for site characterization. *Geophysics* 84(2):B181–B193

27. Flores Orozco A, Kemna A, Oberdörster C, Zschornack L, Leven C, Dietrich P, Weiss H (2012) Delineation of subsurface hydrocarbon contamination at a former hydrogenation plant using spectral induced polarization imaging. *J Contam Hydrol* 136:131–144
28. Flores Orozco A, Kemna A, Zimmermann E (2012) Data error quantification in spectral induced polarization imaging. *Geophysics* 77(3):E227–E237
29. Flores Orozco A, Micić V, Bucker M, Gallistl J, Hofmann T, Nguyen F (2019) Complex-conductivity monitoring to delineate aquifer pore clogging during nanoparticles injection. *Geophys J Int* 218(3):1838–1852
30. Flores Orozco A, Velimirovic M, Tosco T, Kemna A, Sapion H, Klaas N, Sethi R, Bastiaens L (2015) Monitoring the injection of microscale zerovalent iron particles for groundwater remediation by means of complex electrical conductivity imaging. *Environ Sci Technol* 49(9):5593–5600
31. Flores Orozco A, Williams KH, Kemna A (2013) Time-lapse spectral induced polarization imaging of stimulated uranium bioremediation. *Near Surf Geophys* 11(5):531–544
32. Flores Orozco A, Williams KH, Long PE, Hubbard SS, Kemna A (2011) Using complex resistivity imaging to infer biogeochemical processes associated with bioremediation of an uranium-contaminated aquifer. *J Geophys Res Biogeosci* 116(G3)
33. Fritsche W, Hofrichter M (2000) Aerobic degradation by microorganisms. In: Klein J (ed) *Environmental processes—soil decontamination*. Wiley-VCH, Weinheim, Germany, pp 146–155
34. Ghattas AK, Fischer F, Wick A, Ternes TA (2017) Anaerobic biodegradation of (emerging) organic contaminants in the aquatic environment. *Water Res* 116:268–295
35. Glover PWJ (2015) 11.04—geophysical properties of the near surface earth: electrical properties. *Treatise Geophys* 89–137
36. Grieger KD, Fjordbøge A, Hartmann NB, Eriksson E, Bjerg PL, Baun A (2010) Environmental benefits and risks of zero-valent iron nanoparticles (nZVI) for in situ remediation: risk mitigation or trade-off? *J Contam Hydrol* 118(3–4):165–183
37. Günther T, Martin T (2016) Spectral two-dimensional inversion of frequency-domain induced polarization data from a mining slag heap. *J Appl Geophys* 135:436–448
38. Hort RD, Revil A, Munakata-Marr J, Mao D (2015) Evaluating the potential for quantitative monitoring of in situ chemical oxidation of aqueous-phase TCE using in-phase and quadrature electrical conductivity. *Water Resour Res* 51(7):5239–5259
39. Hördt A, Bairlein K, Bielefeld A, Bucker M, Kuhn E, Nordsiek S, Stebner H (2016) The dependence of induced polarization on fluid salinity and pH, studied with an extended model of membrane polarization. *J Appl Geophys* 135:408–417
40. Johansson S, Fiandaca G, Dahlin T (2015) Influence of non-aqueous phase liquid configuration on induced polarization parameters: conceptual models applied to a time-domain field case study. *J Appl Geophys* 123:295–309
41. Johnson TC, Thomle J (2018) 3-D decoupled inversion of complex conductivity data in the real number domain. *Geophys J Int* 212(1):284–296
42. Karaoulis M, Revil A, Tsourlos P, Werkema DD, Minsley BJ (2013) IP4DI: a software for time-lapse 2D/3D DC-resistivity and induced polarization tomography. *Comput Geosci* 54:164–170
43. Kaufmann O, Deceuster J (2007) A 3D resistivity tomography study of a LNAPL plume near a gas station at Brugelette (Belgium). *J Environ Eng Geophys* 12(2):207–219
44. Kemna A (2000) Tomographic inversion of complex resistivity—theory and application. Ruhr-University of Bochum, Ph.D.
45. Kemna A, Binley A, Cassiani G, Niederleithinger E, Revil A, Slater L, Williams KH, Flores Orozco A, Haegel FH, Hördt A, Kruschwitz S (2012) An overview of the spectral induced polarization method for near-surface applications. *Near Surf Geophys* 10(6):453–468
46. Kim B, Nam MJ, Kim HJ (2018) Inversion of time-domain induced polarization data based on time-lapse concept. *J Appl Geophys* 152:26–37
47. Klonowski MR, Breedveld GD, Aagaard P (2008) Spatial and temporal changes of jet fuel contamination in an unconfined sandy aquifer. *Water Air Soil Pollut* 188(1–4):9–30

48. LaBrecque D, Daily W (2008) Assessment of measurement errors for galvanic-resistivity electrodes of different composition. *Geophysics* 73(2):F55–F64
49. LaBrecque DJ, Miletto M, Daily W, Ramirez A, Owen E (1996) The effects of noise on Occam's inversion of resistivity tomography data. *Geophysics* 61(2):538–548
50. Lesparre N, Robert T, Nguyen F, Boyle A, Hermans T (2019) 4D electrical resistivity tomography (ERT) for aquifer thermal energy storage monitoring. *Geothermics* 77:368–382
51. Löser C, Seidel H, Zehnsdorf A, Stottmeister U (1998) Microbial degradation of hydrocarbons in soil during aerobic/anaerobic changes and under purely aerobic conditions. *Appl Microbiol Biotechnol* 49(5):631–636
52. Martin T, Günther T, Flores Orozco A, Dahlin T (2020) Evaluation of spectral induced polarization field measurements in time and frequency domain. *J Appl Geophys* 180:104141
53. Maurya PK, Fiandaca G, Christiansen AV, Auken E (2018) Field-scale comparison of frequency-and time-domain spectral induced polarization. *Geophys J Int* 214(2):1441–1466
54. Mewafy FM, Werkema DD Jr, Atekwana EA, Slater LD, Aal GA, Revil A, Ntarlagiannis D (2013) Evidence that bio-metallic mineral precipitation enhances the complex conductivity response at a hydrocarbon contaminated site. *J Appl Geophys* 98:113–123
55. Nguyen F, Ghose R, Isunza Manrique I, Robert T, Dumont G (2018) Managing past landfills for future site development: a review of the contribution of geophysical methods. In: *Proceedings of the 4th international symposium on enhanced landfill mining*, pp 27–36
56. Olhoeft GR (1985) Low-frequency electrical properties. *Geophysics* 50(12):2492–2503
57. Pelton WH, Ward SH, Hallof PG, Sill WR, Nelson PH (1978) Mineral discrimination and removal of inductive coupling with multifrequency IP. *Geophysics* 43(3):588–609
58. Placencia-Gómez E, Parviainen A, Hokkanen T, Loukola-Ruskeeniemi K (2010) Integrated geophysical and geochemical study on AMD generation at the Haveri Au–Cu mine tailings, SW Finland. *Environ Earth Sci* 61(7):1435–1447
59. Revil A, Coperey A, Mao D, Abdulsamad F, Ghorbani A, Rossi M, Gasquet D (2018) Induced polarization response of porous media with metallic particles—Part 8: influence of temperature and salinity. *Geophysics* 83(6):E435–E456
60. Revil A, Florsch N (2010) Determination of permeability from spectral induced polarization in granular media. *Geophys J Int* 181(3):1480–1498
61. Revil A, Schmutz M, Batzle ML (2011) Influence of oil wettability upon spectral induced polarization of oil-bearing sands. *Geophysics* 76(5):A31–A36
62. Revil A, Skold M (2011) Salinity dependence of spectral induced polarization in sands and sandstones. *Geophys J Int* 187(2):813–824
63. Rücker C, Günther T, Wagner FM (2017) pyGIMLi: an open-source library for modelling and inversion in geophysics. *Comput Geosci* 109:106–123
64. Sauck WA (2000) A model for the resistivity structure of LNAPL plumes and their environs in sandy sediments. *J Appl Geophys* 44(2–3):151–165
65. Schmutz M, Revil A, Vaudelet P, Batzle M, Viñao PF, Werkema DD (2010) Influence of oil saturation upon spectral induced polarization of oil-bearing sands. *Geophys J Int* 183(1):211–224
66. Schmutz M, Blondel A, Revil A (2012) Saturation dependence of the quadrature conductivity of oil-bearing sands. *Geophys Res Lett* 39(3)
67. Schwartz N, Huisman JA, Furman A (2012) The effect of NAPL on the electrical properties of unsaturated porous media. *Geophys J Int* 188(3):1007–1011
68. Schwartz N, Furman A (2012) Spectral induced polarization signature of soil contaminated by organic pollutant: experiment and modeling. *J Geophys Res Solid Earth* 117(B10)
69. Shefer I, Schwartz N, Furman A (2013) The effect of free-phase NAPL on the spectral induced polarization signature of variably saturated soil. *Water Resour Res* 49(10):6229–6237
70. Slater L, Binley A (2006) Synthetic and field-based electrical imaging of a zerovalent iron barrier: implications for monitoring long-term barrier performance. *Geophysics* 71(5):B129–B137
71. Soupios P, Ntarlagiannis D (2017) Characterization and monitoring of solid waste disposal sites using geophysical methods: current applications and novel trends. In: *Modelling trends*

- in solid and hazardous waste management. Springer, Singapore, pp 75–103. https://doi.org/10.1007/978-981-10-2410-8_5
72. Sparrenbom CJ, Åkesson S, Johansson S, Hagerberg D, Dahlin T (2017) Investigation of chlorinated solvent pollution with resistivity and induced polarization. *Sci Total Environ* 575:767–778
 73. Sumner JS (1976) Principles of induced polarization for geophysical prospecting. Elsevier, Amsterdam
 74. Tsourlos P, Vargemezis GN, Fikos I, Tsokas GN (2014) DC geoelectrical methods applied to landfill investigation: case studies from Greece. *First Break* 32(8):81–89
 75. Ustra A, Slater L, Ntarlagiannis D, Elis V (2012) Spectral induced polarization (SIP) signatures of clayey soils containing toluene. *Near Surf Geophys* 10(6):503–515
 76. Velimirovic M, Tosco T, Uyttebroek M, Luna M, Gastone F, De Boer C, Klaas N, Sapion H, Eisenmann H, Larsson PO, Braun J (2014) Field assessment of guar gum stabilized microscale zerovalent iron particles for in-situ remediation of 1, 1, 1-trichloroethane. *Journal Contam Hydrol* 164:88–99
 77. Wang TP, Chen CC, Tong LT, Chang PY, Chen YC, Dong TH, Liu HC, Lin CP, Yang KH, Ho CJ, Cheng SN (2015) Applying FDEM, ERT and GPR at a site with soil contamination: a case study. *J Appl Geophys* 121:21–30
 78. Weller A, Zhang Z, Slater L (2015) High-salinity polarization of sandstones. *Geophysics* 80(3):D309–D318
 79. Yang C, Liu S, Feng Y, Yang H (2018) Influence of electrode polarization on the potential of DC electrical exploration. *J Appl Geophys* 149:63–76